Improved Parameterizations of Vertical Ice-Ocean Boundary Layers and Melt Rates

Ken Zhao[1], Eric Skyllingstad[2], and Jonathan D Nash[1]

[1]Oregon State University
[2]Oregon State University, Oregon

August 12, 2023

Abstract

Buoyancy fluxes and glacial melt rates at vertical ice-ocean interfaces are commonly parameterized using theories derived for unbounded free plumes. A Large Eddy Simulation is used to analyze the disparate dynamics of free plumes and wall-bounded plumes; the distinctions between the two are supported by recent theoretical and experimental advances and demonstrate that unbounded plume theory does not adequately represent plume/boundary layer dynamics at ice-ocean interfaces. Modifications to parameterizations consistent with these simulations are tested and compared to results from numerical and laboratory experiments of meltwater plumes. These modifications include 50\% weaker entrainment and a distinct plume-driven friction velocity in the shear boundary layer up to 8 times greater than the externally-driven friction velocity. Using these modifications leads to 40 times the ambient melt rate predicted by commonly used parameterizations at vertical glaciers faces, which is consistent (and necessary for consistency) with observed melt rates at LeConte Glacier, Alaska.

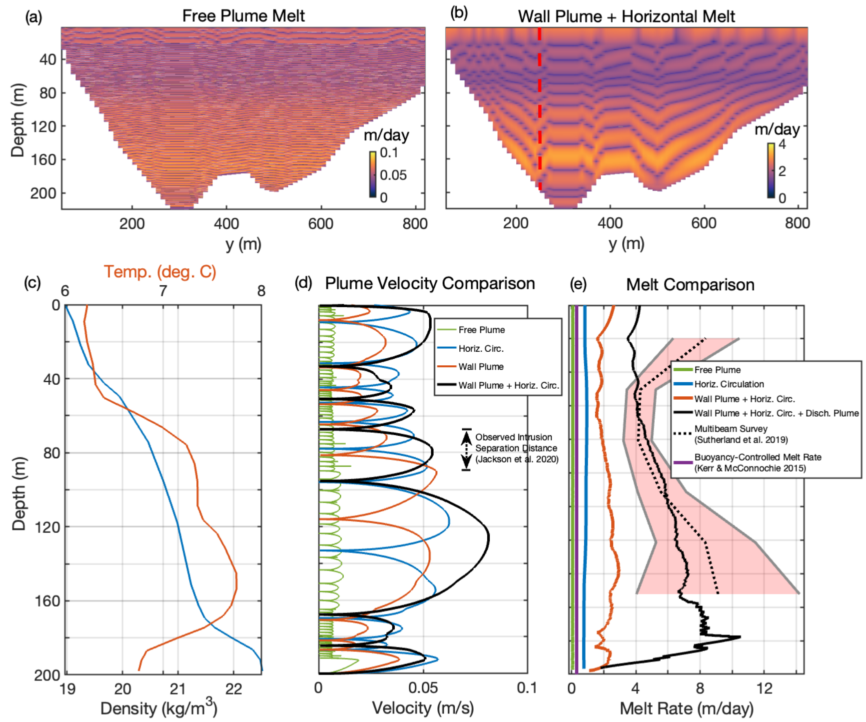
(a)
Free Plume Melt
(b)
Wall Plume + Horizontal Melt
Depth (m)
y (m)
m/day
(c)
Temp. (deg. C)
Density (kg/m3)
(d)
Plume Velocity Comparison
Free Plume
Horiz. Circ.
Wall Plume
Wall Plume + Horiz. Circ.
Observed Intrusion Separation Distance (Jackson et al. 2020)
Velocity (m/s)
(e)
Melt Comparison
Free Plume
Horiz. Circulation
Wall Plume + Horiz. Circ.
Wall Plume + Horiz. Circ. + Disch. Plume
Multibeam Survey (Sutherland et al. 2019)
Buoyancy-Controlled Melt Rate (Kerr & McConnochie 2015)
Melt Rate (m/day)

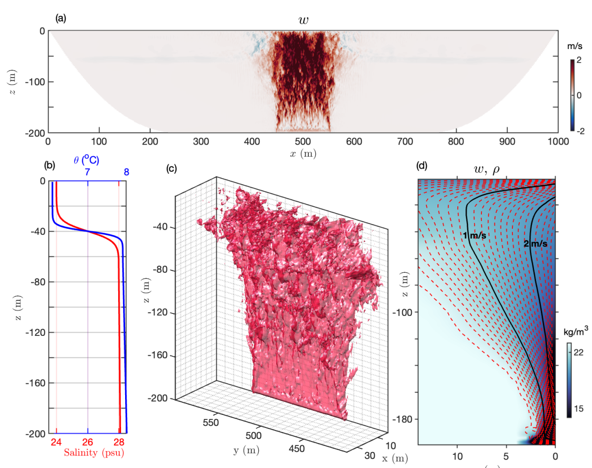
(a)
w
z (m)
x (m)
m/s
(b)
θ (°C)
z (m)
Salinity (psu)
(c)
z (m)
y (m)
x (m)
(d)
w, ρ
1 m/s
2 m/s
kg/m3
z (m)
x (m)

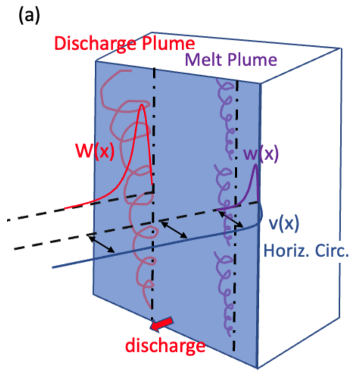

(b)	Drag Coefficient (C_d)	Entrainment (α)	References
Discharge Wall Plume	0.012 - 0.018	0.065 - 0.085	Parker et al. 2021, Greela et al. 1975, Lai et al. 1987, Sangras et al. 2000
Melt Wall Plume	0.12 - 0.18	0.06 - 0.079	Parker et al. 2021, Gayen et al. 2016, Kerr et al. 2015, Cheesewright 1968
Horizontal Circulation	0.0025	-	McPhee et al. 1987, Jenkins 2011, many others
Free Plume (Line)	0.0025	0.10 - 0.13	Jenkins 2011, Cowton et al. 2015, many others

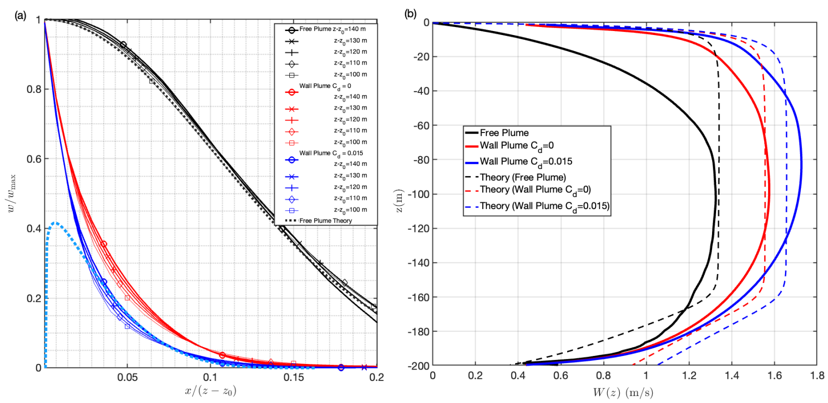

Improved Parameterizations of Vertical Ice-Ocean Boundary Layers and Melt Rates

Ken X. Zhao[1], **Eric D. Skyllingstad**[1], **and Jonathan D. Nash**[1]

[1]College of Earth, Ocean, and Atmospheric Sciences, Oregon State University, 2651 SW Orchard Ave., Corvallis, OR 97331-5503.

Key Points:

- A modified wall-bounded plume parameterization motivated by recent numerical/lab work is proposed as an alternative to free plume theory.
- Subglacial discharge plume simulations at a vertical ice face are consistent with entrainment/plume dynamics from wall-bounded plume theory.
- Melt parameterizations using updated theory is consistent with observations, which is 40 times greater than current parameterizations.

Corresponding author: Ken X. Zhao, `zhaoke@oregonstate.edu`

Abstract

Buoyancy fluxes and glacial melt rates at vertical ice-ocean interfaces are commonly parameterized using theories derived for unbounded free plumes. A Large Eddy Simulation is used to analyze the disparate dynamics of free plumes and wall-bounded plumes; the distinctions between the two are supported by recent theoretical and experimental advances and demonstrate that unbounded plume theory does not adequately represent plume/boundary layer dynamics at ice-ocean interfaces. Modifications to parameterizations consistent with these simulations are tested and compared to results from numerical and laboratory experiments of meltwater plumes. These modifications include 50% weaker entrainment and a distinct plume-driven friction velocity in the shear boundary layer up to 8 times greater than the externally-driven friction velocity. Using these modifications leads to 40 times the ambient melt rate predicted by commonly used parameterizations at vertical glaciers faces, which is consistent (and necessary for consistency) with observed melt rates at LeConte Glacier, Alaska.

Plain Language Summary

Over the past two decades, the outward flow of tidewater glaciers has accelerated, which has contributed to sea level rise. There is growing evidence that this acceleration has been triggered by melting at ice-ocean interfaces, where the ocean comes into contact with and drives the melting of glaciers. In particular, commonly used models and theories describing the ocean turbulence and melt dynamics at vertical ice-ocean interfaces underestimate observed melt rates by an order of magnitude. This study tests proposed changes to existing theories and uses a turbulence-resolving ocean model to validate this alternative (plume with a wall) theory instead of commonly used (plume without a wall) theories; the first type better is more appropriate and takes into account how ocean turbulence drives the melting of a vertical ice wall. We show that these proposed changes are consistent with existing melt observations and are an important step towards understanding a critical process that may help us improve sea level rise predictions.

1 Introduction

Outflowing of marine-terminating glaciers at the margins of the Greenland Ice Sheet and Antarctic Ice Sheet has accelerated in recent years (van den Broeke et al., 2016). A major cause of the accelerated melting is postulated to be the warming of deep ocean currents that come into contact with the termini of tidewater glaciers leading to submarine melt (Holland et al., 2008; Straneo & Heimbach, 2013; Wood et al., 2018; Cowton et al., 2018).

At vertical or near-vertical glacier faces, submarine melt is primarily driven by a combination of three dynamical processes: subglacial discharge plumes, ambient melt plumes, and horizontal circulation (Straneo & Cenedese, 2015; Jackson et al., 2019). The first two types of melt are driven by buoyant plume convection of different strengths with vertical velocities reaching 2–3 m/s for subglacial discharge plumes and up to 10 cm/s for melt plumes. The horizontal near-glacier velocity has a magnitude of up to tens of cm/s, varies significantly between fjords and seasons with limited direct observations (Sutherland et al., 2014; Straneo & Cenedese, 2015; Jackson et al., 2019). Although subglacial discharge plumes have the potential to drive the fastest melt rates locally, they are often observed to occupy a small fraction of the glacial face, while the other two melt processes occur across the entire glacial face (Cowton et al., 2015; Slater et al., 2018).

Recent studies have discussed the relative importance of these three melt processes (Slater et al., 2018; Jackson et al., 2019) and most studies using current parameterizations predict ambient melt rates outside of subglacial discharge plumes to be low (much less than a meter/day, often cms per day; Fried et al. (2015); Carroll et al. (2016); Zhao et al. (2021)). However, there is a mismatch between recent observations and these parameterizations; measured ambient melt rates are an order of magnitude greater (1-10 meters/day) across the entire submarine terminus, even in parts of the glacier face far from discharge plumes (Jackson et al., 2019; Sutherland et al., 2019). In addition to the discrepancy for ambient melt rates, because discharge plumes often cover a small fraction of the total glacier area, the face-averaged and total observed melt rates are also much higher than those predicted by existing parameterizations.

In this study, we extend results from a recently proposed parameterization for vertical glacial ice fronts, which proposed modifying unbounded plume theory using empirical constraints for the efficiency of turbulent heat and salt transfer to match observational data (Schulz et al., 2022). Schulz et al. (2022) also proposed a transfer function that merges the velocity-dependent (shear-dominated) and velocity-independent (buoyancy-dominated) melt regimes, albeit with a significantly higher buoyancy-dominated melt rate than previous literature (e.g., Kerr and McConnochie (2015)). In this study, we propose a physically-motivated melt parameterization that includes both convective- and shear-dominated melt regimes that is consistent with existing theories, observations, and laboratory experiments.

In section 2, we present an updated and integrated overview of free plumes, wall-bounded plumes, and horizontal circulation-driven melt, and how each drive the boundary layer dynamics and melt at a vertical ice face. In section 3, we present a set of Large Eddy Simulations of a subglacial discharge plume with and without a vertical glacier wall to compare the horizontal and vertical profiles of vertical momentum for unbounded free plumes and wall-bounded plumes. This is compared with existing theories for discharge plumes. In section 4, we compare the existing parameterizations of glacial melt rates at a rapidly melting vertical ice face (LeConte, Alaska) with the updated melt plume theory (section 2) and discharge plume theory (section 3). This shows that wall-bounded plume theory (after accounting for buoyancy due to melt from horizontal circulation) is consistent with recent observations, while the commonly used free plume theory underpredicts the melt rate outside of discharge plumes by a factor of 40. Finally, we summarize our key findings and proposed changes to vertical ice-ocean interface parameterizations and conclude.

2 Theory of Vertical Ice-Ocean Interfaces

In this section, we summarize and integrate recent developments in vertical ice-ocean boundary layer parameterizations by first discussing the thermodynamic coupling of the interfacial boundary layer to the corresponding (plume- or external forcing-driven) outer velocity, temperature, and salinity. We then discuss how these outer properties are parameterized for each of the three types of outer boundary layers: subglacial discharge plumes, ambient face-wide melt plumes, and background/external circulation. We refer the reader to recent reviews of glacial plumes and ice-ocean parameterizations for further details and references (Malyarenko et al., 2020; Hewitt, 2020).

2.1 Vertical Ice-Ocean Boundary Layers

Current melt rate parameterizations at vertical ice-ocean interfaces can be classified into being relevant in either the buoyancy-driven regime (Kerr & McConnochie, 2015) or the shear-driven regime (McPhee et al., 2008; Jenkins, 2011) based on whether the rate of turbulent heat flux is primarily driven or constrained by buoyancy flux diffusing away from the wall (buoyancy-driven) or the momentum flux diffusing towards the wall (shear-driven); a transition from the first to the second regime occurs if the buoyant updraft has gained significant vertical momentum (Wells & Worster, 2008). In the absence of externally-forced circulation or turbulence, vertical ice-ocean interfaces start off as wholly laminar boundary layers within the first 10–30 cm above their initiation point before they transition to the buoyancy-driven turbulent regime (Josberger & Martin, 1981; Wells & Worster, 2008); however, we do not discuss the laminar regime further due to its limited relevance to the geophysical scale of glaciers.

Within buoyancy-driven boundary layers, the melt rate is velocity-independent and can be approximated as (Kerr & McConnochie, 2015)

$$m_B = 0.25(T - T_f(S))^{4/3}, \text{ for } Ra < R_c \tag{1}$$

(in μm ^{o}C$^{-4/3}$ s^{-1}) where T is the ambient temperature, T_f is the local freezing temperature (which can be calculated using the liquidus condition similarly to SI Eq. (7c)) at ambient salinity S. For shear boundary layers,

$$m_S = c_w \gamma_T (T - T_b)\hat{L}^{-1}, \text{ for } Ra > R_c\,, \tag{2}$$

and $\hat{L} \equiv L + c_i(T_b - T_i)$. Here, $c_w = 3974$ J kg/^{o}C and $c_i = 2009$ J kg/^{o}C are the specific heat capacity of water and ice, respectively, $L = 3.35 \times 10^5$ J/kg is the latent heat of ice, γ_T is the turbulent thermal transfer coefficient (with units of velocity), and T_b is the boundary layer temperature predicted by solving the 3-equation thermodynamical balance (see SI S-1). In the case of LeConte glacier, which is abutted by warm fjord waters (up to 8 ^{o}C), T_i is nearly 0 ^{o}C. The turbulent transfer coefficient is dependent on the friction velocity and is discussed in the next subsection.

Here, the threshold between buoyancy-driven and shear-driven boundary layers is set by a critical value of the buoyancy Rayleigh number $Ra = b(z - z_0)^3/(\nu\kappa)$, which represents the plume's increasing convective efficiency with respect to diffusion with height from the source $(z - z_0)$, where $\nu = 1.8 \times 10^{-6}$ m^2/s is the viscosity and $\kappa = 7.2 \times 10^{-10}$ m^2/s the salt diffusivity of seawater. The critical Rayleigh number Ra_c for the transition and its corresponding transition height $z_c - z_0$ is the subject of some debate (Grossmann & Lohse, 2000; Wells & Worster, 2008), partly due to the fact that this transition has not been observed in a natural setting, but it is postulated to occur at $Ra_c = 10^{21}$ (Kerr & McConnochie, 2015). Recent laboratory experiments suggest that this occurs at a vertical velocity of 0.03 to 0.05 m/s for a discharge plume at 3.5 °C above freezing (McConnochie & Kerr, 2017a). A simple way to combine the two regimes in Eqs. (1) and (2) is to use a melt rate prediction based on the dominant turbulent transfer process at the boundary layer, resulting in

$$m = \max\{m_S, m_B\}\,. \tag{3}$$

2.2 Shear-Driven Turbulent Transfer

The turbulent transfer coefficient in a shear-dominated regime is commonly expressed in terms of horizontal (v) and vertical (w) near-glacier ocean velocities as

$$\gamma_T = \underbrace{\sqrt{C_d}\Gamma_T}_{St} \sqrt{v^2 + w^2}\,, \tag{4}$$

with a drag coefficient C_d ranging from 0.001 to 0.0097. See Fig. 1a for a schematic of the different boundary layers and corresponding velocities. In the absence of boundary layer observations, a commonly used placeholder value of $C_d = 0.0025$ is used in the ice plume literature along with a turbulent heat transfer constant $\Gamma_T = 0.022$ (Jenkins et al., 2010). However, this does not distinguish between the frictional boundary layer thickness (via C_d) in the horizontal and vertical and more important, it does not distinguish between the external velocity-field driven shear boundary layers and the plume-driven boundary layers. For melt plumes and discharge plumes, it is also unclear how v and w should be defined as both far-field velocities for plumes are zero.

The total shear stress at a shear boundary layer is the sum of both the viscous and turbulent shear stresses

$$\frac{\tau}{\rho} = \underbrace{\nu \partial_x \overline{w}}_{\text{viscous stress}} - \underbrace{\overline{u'w'}}_{\text{Reynolds stress}} . \tag{5}$$

In most externally-forced wall-bounded shear flows (in either the atmospheric boundary layer or horizontal ice-ocean boundary layers; Jenkins (1991); Kaimal and Finnigan (1994); Pope (2000)), the turbulent Reynolds stress dominates the momentum dissipation contribution. However, recent laboratory and numerical experiments suggest that plume-driven buoyancy forcing at an ice-ocean interface behaves differently than the external far field-forced velocity field. This is because buoyancy (from melting) is generated directly at the interface itself in melt plumes or close to the wall in the case of subglacial discharge plumes (Gayen et al., 2016; Parker et al., 2020, 2021). Therefore, it is important to distinguish shear stresses associated with the external velocity field from those of the internal plume-driven shear stresses. For both melt plumes and discharge plumes, more of the shear stress contribution is viscous in Eq. (5) and thus, more of the kinetic energy is dissipated before becoming turbulent.

However, this has been demonstrated to lead to a melt rate that scales strongly with the friction velocity of the shear boundary layer (Gayen et al. (2016); McConnochie and Kerr (2017b); Parker et al. (2020, 2021)). In order to separate the individual contributions of plume-driven shear and externally-driven shear, we express the turbulent thermal transfer coefficient (and similarly for the turbulent salinity transfer coefficient) as

$$\gamma_T = \Gamma_T \left(v_*^2 + w_*^2 \right) , \tag{6}$$

where the plume-driven friction velocity is defined such that $w_*^2 = \nu \left. \partial_x \overline{w_p} \right|_{x=0}$ at a vertical wall $x = 0$, for a time-averaged plume vertical velocity w_p (which assumes all of the viscous stress is converted to turbulent stress). Eq. (6) is a simple way of combining the horizontal and vertical components friction velocity via the velocity magnitude, which is commonly used when there is a 2D external velocity field (Jenkins, 2011), but such an expression has not been validated for combining plume-driven friction velocity and externally-driven friction velocity (see McConnochie and Kerr (2017b) for further discussion).

In previous studies, the plume-driven shear boundary layer is often expressed using an equivalent skin friction coefficient $C_d^{\mathrm{p}} \equiv w_*^2/W_p^2$ with empirically derived estimates that are significantly higher than its analogously-defined externally-forced counterpart $C_d^{\mathrm{p}} \equiv v_*^2/v_\infty^2$ for a far-field velocity v_∞ ($C_d^{\mathrm{ext}} \approx 0.0025$, whereas $C_d^{\mathrm{p}} \approx 0.015$ for discharge plumes, and $C_d^{\mathrm{p}} \approx 0.15$ for melt plumes; Gayen et al. (2016); Parker et al. (2020, 2021)). The characteristic plume velocity W_p used in this parameterization is defined as the horizontally-integrated mass flux divided by momentum flux (see supplemental material S-1.2 for further discussion).

2.3 Theory of Unbounded Free Plumes

We first discuss buoyant plume convection in the absence of a wall, which is an extensively studied subject (Morton et al., 1956; Turner, 1979). A 1D theory for the vertical (along-plume) variation in characteristic vertical velocity $W(z) = W_p(z)$, buoyancy $B(z)$, and plume width $D(z)$ can be solved using the Boussinesq conservation laws of mass, momentum, and buoyancy, and empirically-derived entrainment assumption (see SI S-1 for further details). Here, $W(z)$ and $B(z)$ are defined as the mean of the vertical velocity w_p and buoyancy $b = -g(\rho - \rho_a)/\rho_0$ over the plume width for a plume density ρ, an ambient density ρ_a, and reference density ρ_0. This theory relies on the empirically-supported assumption originating from Morton et al. (1956), that the local time-mean entrainment at each depth is proportional to the characteristic vertical velocity $W(z) = -\alpha U(z)$ for a horizontal inflow velocity magnitude $U(z)$ and constant entrainment coefficient α.

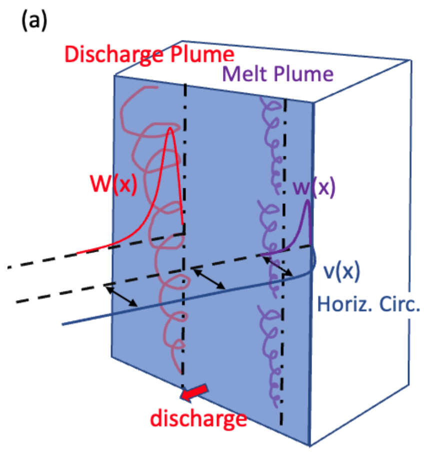

(b)	Drag Coefficient (C_d)	Entrainment (α)	References
Discharge Wall Plume	0.012 - 0.018	0.065 - 0.085	Parker et al. 2021, Greela et al. 1975, Lai et al. 1987, Sangras et al. 2000
Melt Wall Plume	0.12 - 0.18	0.06 - 0.079	Parker et al. 2021, Gayen et al. 2016, Kerr et al. 2015, Cheesewright 1968
Horizontal Circulation	0.0025	-	McPhee et al. 1987, Jenkins 2011, many others
Free Plume (Line)	0.0025	0.10 - 0.13	Jenkins 2011, Cowton et al. 2015, many others

Figure 1. (a) An overview schematic of wall-bounded discharge and melt plume and the ice-ocean boundary layer. The horizontal and vertical velocity profiles for the discharge plume and melt plume ($v(x)$, $W(x)$, and $w(x)$, respectively) are illustrative and not to scale. (b) A table of reference ranges of drag coefficient C_d and plume entrainment coefficient α corresponding to the three types of ice-ocean boundary layers compared to the commonly-used free plume parameterization and their references.

For plumes at an ice-ocean interface, this has been modified to include an accounting of the heat budget, which is a necessary component in calculating the melt rate in Eq. (1) or (2). Therefore, we have the following commonly-used system of equations for 1D line plume evolution originating from Jenkins (1991)

$$\frac{\partial(DW)}{\partial z} = \alpha W + m\,, \tag{7a}$$

$$\frac{\partial(DW^2)}{\partial z} = DB - C_d^{\mathrm{p}} W^2\,, \tag{7b}$$

$$\frac{\partial(DWT)}{\partial z} = \alpha W T_a + m T_{\mathrm{ef}}\,, \tag{7c}$$

$$\frac{\partial(DWS)}{\partial z} = \alpha W S_a + m S_i\,. \tag{7d}$$

where m is the melt rate, S_i is the ice salinity and each of the parenthetical terms are integrated numerically in z to generate the 1D plume solution (see SI S-1 for a derivation). Note that m and the effective thermal gradient T_{ef} (i.e., the boundary layer temperature and salinity) must be calculated using 3-equation thermodynamics (see SI S-1). This 1D plume theory has been used extensively in the parameterizations of vertical ice faces (Jenkins, 2011; Cowton et al., 2015; Slater et al., 2018; Jackson et al., 2017, 2019; Sutherland et al., 2019; Zhao et al., 2021) due to its simplicity.

Note that this system of equations is valid for both discharge plumes (for an appropriate initial mass and momentum) and melt plumes (for approximately zero initial mass and momentum). These equations can be modified slightly to describe a point source (by replacing plume width D with plume radius R and deriving the appropriate conservation laws for a radial symmetry). However, line discharge plumes (a finite width buoyancy source instead of a point source) have been shown to better reproduce existing near glacier melt fraction observations, but this may be more attributed to the source width parameter instead of the dynamics (Jackson et al., 2017).

For comparison with wall-bounded plume profiles discussed in the next subsection, the commonly used velocity profile $w(x)$ for free plumes has been determined experimentally and is well-charaterized by a Gaussian curve (Ramaprian (1989), Paillat and Kaminski (2014); suggestive of a random walk of water mass parcels)

$$w(\hat{x}) = W_{\max}(z) \exp\left(\frac{-\hat{x}^2}{D^2}\right), \tag{8}$$

where $\hat{x} = x/(z - z_0)$ is the z-scaled x coordinate (such that the plume profiles $w(\hat{x})/W_{\max}(z)$ collapse to a single characteristic profile by similarity with height from the source, $z - z_0$) and the maximum plume velocity at the plume centerline $W_{\max} \approx 1.35W$.

Although the line plume theory momentum flux equation in Eq. (7b) from Jenkins (1991) includes a skin friction term at the wall, C_d^{p} has a confusing interpretation if a wall does not exist as its value depends on the wall-bounded shear boundary layer vertical velocity profile and the boundary layer width. This term owes its commonly used value of 0.0025 in ice-ocean applications largely to observations at weakly melting nearly horizontal ice-ocean interfaces (McPhee et al., 1987; Jenkins et al., 2010), which have boundary layers that can be well-approximated by Monin-Obukhov theory (Vreugdenhil & Taylor, 2019); this value of skin friction is also commonly used in most other passive surfaces.

2.4 Theory of Wall-Bounded Plumes

In the presence of a vertical wall, the 1D line plume theory in Eqs. (7a)–(7d) still holds with a drag coefficient C_d^{p} that can now be diagnosed experimentally or numerically via the balance of bulk momentum balance terms in Eq. (7b). In a wall-bounded plume with a shear layer, the across-plume gradients determined experimentally and numerically differ greatly from the Gaussian-shaped vertical momentum profiles of free plumes and as a result, different distributions of horizontal turbulent fluxes of momentum and buoyancy (Sangras et al., 2000; Parker et al., 2020, 2021).

These disparities are owed to two major differences between a plume convecting along a wall vs. one without a wall: the impermeability condition (u at the wall is zero) and the no-slip condition (w at the wall is zero). Experiments have shown that the impermeability condition leads to reduced eddy meandering and weaker mixing of buoyant fluid away from the wall. This produces higher near-wall vertical momentum, which together with the no-slip condition contribute to significantly higher shear stresses (Parker et al., 2020, 2021). For discharge plumes, the shear stress diagnosed from laboratory and numerical experiments exerts a drag on momentum equivalent to 15% of the buoyancy force for discharge plumes (Parker et al., 2020) and 65% of the buoyancy force for melt plumes in small (1 meter tall), unstratified domain heights (Gayen et al., 2016; Parker et al., 2021). These experimentally-derived estimates imply a drag coefficient of $C_d^{\mathrm{p}} = 0.015$ for discharge plumes, and $C_d^{\mathrm{p}} = 0.15$ for melt plumes along with significantly lower entrainment: $\alpha = 0.075$ for discharge plumes, and $\alpha = 0.068$ for melt plumes. See Fig. 1b for a list of the drag coefficients, entrainment, and a corresponding list of references.

A significant body of experimental and theoretical work supports an across-plume vertical velocity profile in the heated wall (free convection literature), which was first approximated in Eckert and Jackson (1950) as

$$w(\hat{x}) = W_{\max}\hat{x}^{1/7}\left(1 - \hat{x}\right)^4. \tag{9}$$

This velocity profile also approximately matches recent experiments of ice-ocean boundary layers (Parker et al., 2021). However, it is unknown how these dynamics play out at much larger Ra and rise heights in the well-developed shear boundary layers (Eq. (2)) due to complications of a much weaker solutal diffusivity (where the Schmidt number $Sc = \nu/\kappa_S \approx 2600$ for seawater), although in theory it is analogous to the large Prandtl $Pr = \nu/\kappa_T$ regime.

2.5 Horizontal Circulation-Driven Melt

The near-glacier horizontal velocity has a very different profile $v(x)$ compared to the across-plume vertical velocity profile $w(x)$ (see Fig. 1a), where the commonly used parameterization uses the far-field background velocity $v(\infty)$ (at 10-100 m away from the boundary) and a drag coefficient of $C_d^{\text{ext}} = 0.0025$ (consistent with a meter scale law-of-the-wall log layer). By comparison, plume-driven shear boundary layers are much thinner (centimeters or less) and they have proportionally larger friction velocities compared to the outer velocity ($C_d^{\text{ext}} = v_*^2/v_\infty^2 \ll C_d^{\text{p}} = w_*^2/W_p^2$).

The far-field velocity $v(\infty)$ may either be observed directly (estimated to be 20 cm/s near the face of LeConte (Jackson et al., 2019)) or parameterized using the theory from Zhao et al. (2021, 2022), which uses a steady state balance between vorticity supplied by the discharge and melt plumes and bottom drag for a given density layer bounded by $z = z_\rho$ and $z_{\rho'}$ as

$$v_n(\infty) \approx \frac{2f\psi}{C_F C_d^{\text{ext}}(z_{\rho'} - z_\rho)} \,. \tag{10}$$

Here ψ is the near-glacier overturning strength (which can be calculated using the plume theory for W and using the entrainment assumption $\partial W(z) = -\alpha U(z)$; see Sections 2.2 and 2.3)

$$\psi = \max_{z'} \int_0^{W_f} \int_{z_{\rho'}}^{z_\rho} U \; \mathrm{d}z' \, \mathrm{d}y' \,, \tag{11}$$

for Coriolis parameter f, fjord width W_f, and the fjord perimeter at the depth of a given density layer C_F. See Zhao et al. (2021, 2022, 2023) for additional details.

3 Large Eddy Simulations of Subglacial Discharge Plumes

Although recent experimental and numerical studies (discussed in Section 2.3, Gayen et al. (2016); Parker et al. (2020, 2021)) demonstrated a larger wall shear stress and weaker entrainment in wall-bounded discharge plumes compared to free plumes, those experiments were not able to diagnose the relative importance of the two wall effects: impermeability and the no-slip boundary condition. In the following experiments, we test the importance of these two effects separately. We examine the horizontal profiles and vertical acceleration of vertical velocity to reconcile the differences (particularly how it is treated in the glacial context) between the theory of unbounded free plumes and wall-bounded plumes.

3.1 Model Setup

To examine the difference between a wall-bounded plume and a free plume, we conduct a series of Large Eddy Simulations (LES) of an idealized near-glacier fjord domain using the Massachusetts Institute of Technology general circulation model (MITgcm; Marshall et al. (1997)). The vertical and horizontal resolution are both 1 m and we use a 3D Smagorinsky viscosity parameterization with a coefficient of 0.03 (Smagorinsky, 1963). The model is forced on the open-ocean side by an idealized temperature/salinity (Fig. 2b) based on August 2016 observations at LeConte Glacier, Alaska (Jackson et al., 2019). For the cases with a vertical wall, we parameterized melting at the ice face using a shear boundary layer assumption and 3-equation thermodynamics (Eqs. (2) and (4)). This differs from many previous studies, which often assume a fixed buoyancy flux with depth (Parker et al., 2020, 2021). We use an idealized bathtub domain with smooth sidewalls (see Fig. 2a for the bathymetric variation in y) for a 200m deep, 1 km wide (in y) by 2 km long (in x) fjord section with a subglacial discharge of 150 m^3/s, which is distributed at the $x = 1$ m boundary as a source of mass inflow. To help initiate turbulent motions near the source, the mass source is distributed at 10 evenly-spaced outlets over a 100 meter extent in y ($450 \leq y \leq 550$ m) at $z = -200$ m, which provides a small degree of along-y asymmetry in vertical momentum without any meaningful influence on the y-integrated vertical momentum. The length of this fjord section minimizes the interaction between the plume-generated turbulence and the open ocean boundary at $x = 2000$ m. See SI S-2 for additional details of the numerical model.

3.2 Simulation Results

Fig. 2a, c, d show the near-face (x=3) vertical velocity, $w = 0.2$ m/s velocity surface, and meridionally-averaged vertical velocity for a reference case of a wall-bounded discharge plume at an ice-ocean boundary without drag. This shows the development of 3D convective turbulence, which develops due to xz-plane vorticity sourced at $y =$ 450, 550 m on the margins of the line plume and throughout the plume due to vorticity aligned in the yz-plane; these regions correspond to high horizontal shear in vertical velocity leading to turbulent shear production. Although a finer grid would better resolve the smaller scales of turbulence at depths especially near the plume source, the turbulence in the upper half of the plume is sufficiently well-developed to calculate across-plume profiles of vertical velocity. Fig. 2d also shows the mean meridionally-averaged density field, whose positive buoyancy anomaly within the plume is the source of the buoyancy flux driving upward acceleration. This also shows the gradual decrease in density along the plume due primarily to the entrainment of ambient water.

To compare the characteristics of free plumes and wall-bounded plumes, we examine three test cases. The first case is a free plume, the second case is a wall plume without drag at the wall, and the third case is a wall plume with a drag coefficient of $C_d =$ 0.015 to emulate the no-slip condition (which is parameterized and not resolved). Note that this value of drag coefficient is determined for discharge plumes (which is distinctly lower than than the effective drag felt by a melt plume) and is obtained experimentally (see Section 2b and Fig. 1b).

Fig. 3a shows the horizontal variation of vertical velocity $w(x)$ and Fig. 3b shows the vertical variation of characteristic vertical velocity $W(z)$ for each of the three test cases. These demonstrate that the dynamics are consistent with their respective theories; free plumes $w(x)$ are well approximated by the Gaussian profiles in Eq. (6) and wall-plume profiles are consistent with the turbulent wall-plume theory in Eq. (7). These functions were fit using α as a free parameter (which determines the characteristic width scale D of the plume for a given $z - z_0$). For the free plume case, this implies $\alpha = 0.14$; for the wall-plume case without drag, $\alpha = 0.083$; for the wall-plume case with drag, $\alpha =$ 0.079. These diagnosed values are consistent with those from previous studies (Fig. 1b).

Fig. 3b shows the vertical variation of the characteristic vertical velocity $W(z)$ along with the corresponding theoretical solutions from 1D plume theory (Eq. (5)). This comparison demonstrates that the bulk mean vertical momentum W is consistently well-predicted by plume theory in these simulations. In particular, 1D plume theory captures the 17% increase in W for the wall-bounded free plume and the smaller 6% increase in W when drag is added (due to the additional buoyancy flux from melt). Note that the characteristic width of the wall-bounded plume is much narrower (in Fig. 3a), partially due to weaker entrainment for the wall-bounded plumes and not as much acceleration of the characteristic vertical velocity, which is consistent with 1D plume theory. A notable caveat here is that near the source of the plume, the plume is not fully resolved at the 1 m horizontal resolution used in these simulations and likely contributes to the small mismatch in vertical momentum there. Near the depth of neutral buoyancy at the top of the plume, there is also a similar discrepancy between the theory and simulations, but this is likely caused by additional sources of mixing/instabilities not captured by the theory at these depths.

In summary, these results show that the presence of a vertical wall strongly alters the dynamics. However, we demonstrate that existing parameterizations (based on the-

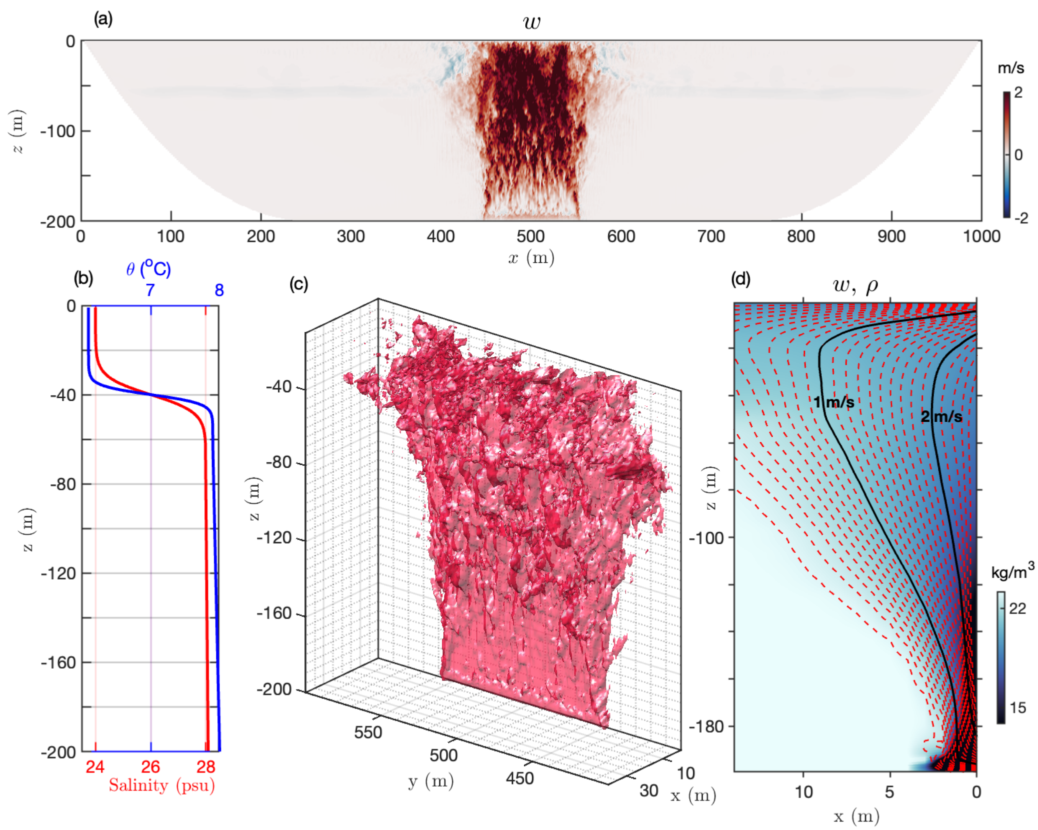

Figure 2. (a) Vertical velocity w (m/s) at $x = 3$ m away from the ice. (b) Open-ocean boundary condition profiles of conservative temperature θ_a and salinity S_a. (c) The vertical velocity surface $w = 0.2$ m/s. (d) Meridionally-averaged vertical velocity contours from 0.0 to 2.3 m/s (orange is 0.1 m/s spacing, black is 1.0 m/s spacing) plotted on density (in color).

ory for unbounded/free plumes), can be adapted to produce the observed variability if a lower entrainment coefficient is used. In addition, the critical difference between the entrainment of free and wall-bounded plumes emerges primarily due to the impermeability condition and to a lesser extent, the no-slip condition, although the latter is implicit in the shear boundary layer parameterization (just not as important for the vertical momentum balance). One caveat of these experiments is that the near-wall horizontal resolution in these LES does not allow the near-glacier plume-driven boundary layer to be fully resolved, which appears to be much more important in melt plumes where the wall shear stress decreases the total plume momentum by approx. 65% in both laboratory experiments and Direct Numerical Simulations (DNS) (Parker et al., 2021; Gayen et al., 2016). The resolution and computational cost required to resolve the laminar boundary layer (in e.g., Gayen et al. (2016)) would not currently be affordable at vertical scales larger than a few meters. Therefore, we cannot simultaneously simulate the large-scale discharge plume dynamics while resolving the dynamics of the melt plumes and viscous/diffusive boundary layers. Instead, the drag coefficient and entrainment rates from small-scale laboratory experiments and DNS (Parker et al., 2021; Gayen et al., 2016) are used to supplement the melt parameterization for melt plume-driven boundary layers in the following section.

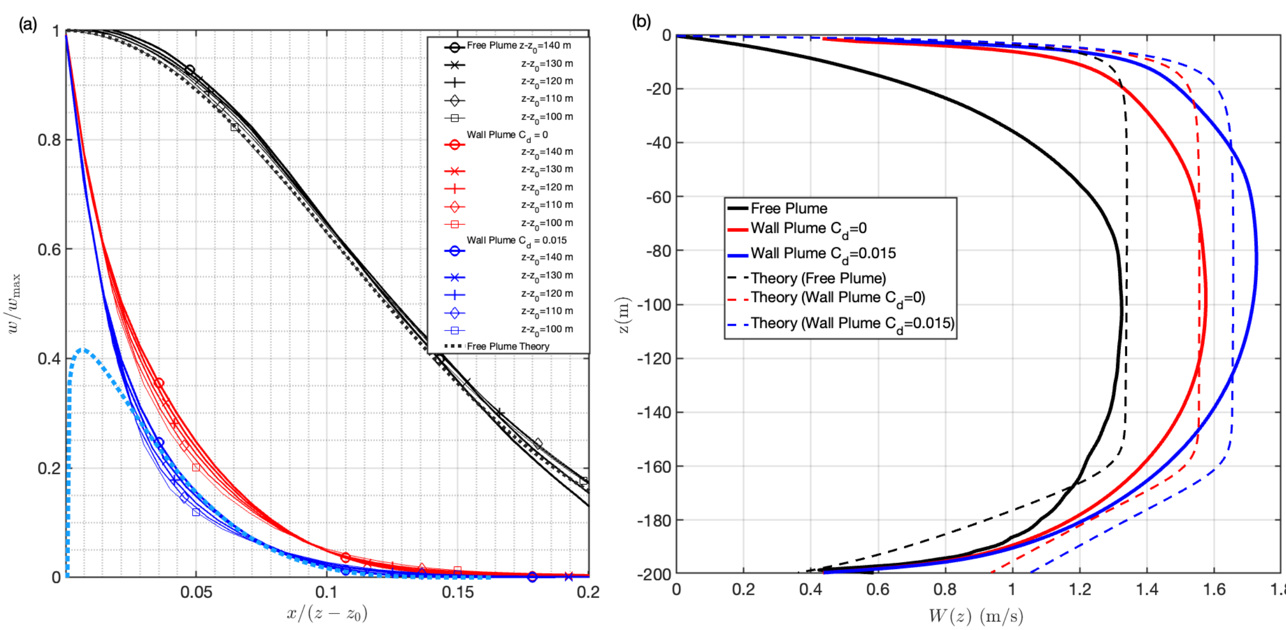

Figure 3. (a) The horizontal variation of vertical velocity $w(x)$ for three test cases: free plume (black), wall-bounded plume without wall drag (red), and wall-bounded plume with wall drag (blue) with theoretical predictions based on Eqs. (8)–(9) for the free plume, and wall-bounded plume with drag case. (b) The vertical variation of characteristic vertical velocity $W(z)$ for each of the three cases in (a) with plume-theory solutions using Eq. (7a)-(7c).

4 Application of Theory to Observations at LeConte Glacier, Alaska

In this section, we apply the synthesized melt and plume theories discussed in Section 2 to observations at a rapidly melting vertical ice face. This is motivated by recent estimates of glacial melt rate using repeat multibeam measurements at LeConte Glacier, Alaska (Sutherland et al., 2019), which observed much larger melt rate estimates than those predicted by prior applications of melt plume theory (Jackson et al., 2019).

Fig. 4 shows a comparison between the melt rate and plume velocity at Leconte Glacier using the temperature and salinity profiles from the August 2016 field campaign (panel c, Sutherland et al. (2019)). This demonstrates a significant difference in melt rate distribution at LeConte glacier calculated using the traditional free plume melt parameterization (panel (a)) vs. the updated wall plume melt parameterization (panel (b)). In particular, the free plume melt paramterizations uses the different representation of the turbulent transfer coefficient in Eq. (4) vs. the updated from Eq. (6), with horizontal melt included (assuming a uniform horizontal velocity of 0.2 m/s). For the updated wall plume melt parameterization (panel (b)), we also use a smaller entrainment coefficient α and much larger $C_d^{\mathrm{p}} = 0.15$ consistent with wall-bounded melt plumes, and the horizontal velocity (which influences the melt rate directly in Eq. (3), but also the 1D plume theory in Eq. (7)). Including these differences results in a maximum melt rate that increases from <0.1 m/day to 2.2 m/day and much larger separation distance between meltwater intrusions (the darker colors in these panels show where plumes intrude/new plumes form; see Jackson et al. (2019) for a discussion of these intrusions). See Fig. S1 in the SI for additional panels that reflect the melt rates for the free plume theory with horizontal circulation and discharge plume scenarios.

The characteristic vertical velocity is shown in panel (d) for 4 different cases: a free plume (with low drag and high entrainment), a free plume with horizontal circulation-driven melt, a wall plume without horizontal circulation, and a wall plume with horizontal circulation. This shows that the including horizontal velocity-driven melt for a free plume and using wall-bounded plume (drag and entrainment) coefficients have similar effects; they increase the vertical velocities from less than 0.01 m/s to 0.04 m/s and also increase the intrusion separation distance by a factor of 5. If a horizontal velocity-driven melt is included for a wall-bounded plume, their combined effects compound for weakly stratified depths (e.g., $z = -170$ to -90), while they do not differ from their component effects for strong stratified depths (e.g., $z = -80$ to -40) since the increased inertia is still not adequate to overcome the background stratification. Note that the wall-bounded plumes and horizontal circulation cases produce reasonable intrusion separation distances comparable to the observations from Jackson et al. (2019) while the free plume coefficients does not.

In panel (e), the meridionally-averaged melt rates from panel (c) is compared with a discharge plume added (black), the melt rate estimates from the repeat multibeam survey, and the buoyancy-controlled melt rate using Eq. (1). The melt rate estimate for buoyancy-controlled boundary layers is shown for comparison (approx. 0.3 m/day using Eq. (1)). For melt plumes, this leads to an overall effect of amplifying melt rates at all depths by a factor of 40, which can be attributed to 8x due to increased C_d^{p} compounded with 5x from the horizontal circulation-driven melt. The horizontal circulation component contributes directly to the melt and buoyancy input (via Eq. (4)), which feeds back on the melt plume's vertical velocity (via Eq. (5)). In the discharge plume case, the buoyancy flux increase is relatively minor ($< 2\%$ since the buoyancy flux from melting is very small compared to the buoyancy flux from the discharge plume), so there is no feedback between the additional melting and vertical momentum of the plume. These higher melt rates leads to proportional higher buoyancy fluxes and overturning circulation within the fjord.

In summary, the total, local melt rates, and meltwater intrusion depths are consistent between the observations and the updated wall plume theory when horizontal circulation is included, while the melt is significantly underpredicted by using free plume theory alone. The melt rates are somewhat underpredicted by using wall-plume theory without horizontal circulation or free plume theory with horizontal circulation.

5 Summary and Conclusions

In this study, we provide evidence to support the claim that wall-bounded plumes very different dynamically from free plumes. We propose an updated parameterization that uses physically-reasonable values for the turbulent transfer coefficients, melt rates, and entrainment for wall bounded plumes and vertical ice-ocean interfaces. We then test the impact and validate (using large eddy simulations and observations) these updated parameterizations.

These differences are summarized as follows: (1) The plume-driven drag coefficient (C_d^{p}) is distinct from the externally forced drag coefficient (C_d^{ext}). Unlike an unstratified flow over a flat plate, C_d^{p} is not a drag coefficient in the classical sense as it does not depend on the roughness of the surface: in these theories it is used as a means of quantifying the buoyancy-driven turbulence and momentum budget. As such, it is necessary to a drag coefficient that is relevant to the dynamics in question. Based on recent numerical and laboratory experiments, estimates of the plume-driven drag coefficients have been proposed for discharge plumes ($C_d^{\mathrm{p}} = 0.015$) and melt plumes ($C_d^{\mathrm{p}} = 0.15$). These differences reflect the different types of boundary layers (i.e., $v(x)$, $w(x)$, and $W(x)$ in Fig. 1). (2) When wall plumes are parameterized, the entrainment coefficient α should use a much smaller value: $\alpha = 0.075$ for discharge plumes and $\alpha = 0.068$ for melt plumes. (3) Horizontal boundary layers $v(x)$ and their melt contribution should still be treated with the usual shear boundary layer width scales consistent with $C_d^{\mathrm{ext}} = 2.5 \times 10^{-3}$. However, it is important to include the effect of this melt within the ambient melt plumes as their dynamics are sensitive to horizontal melt rates.

Currently, buoyancy fluxes and glacial melt rates at vertical ice-ocean interfaces are commonly parameterized using theories for unbounded free plumes and assume a universal drag coefficient. However, both Direct Numerical Simulations and laboratory experiments suggest that wall-bounded plumes leads to different plume entrainment and vertical velocity profiles (with differences between subglacial discharge and melt plumes) due to the presence of a shear boundary layer. In addition, a recently data-supported parameterization of the turbulent transfer function that merges the velocity-dependent and -independent (buoyancy-dominated) melt regimes (Schulz et al., 2022) found a significantly higher baseline buoyancy-dominated melt rate than previous literature (e.g., Kerr and McConnochie (2015)). Our study reconciles these inconsistencies using a physically-motivated melt parameterization that includes both convective- and shear-dominated melt regimes and is broadly consistent with existing observations, laboratory experiments, and field data.

We compare the predictions of free plume and wall-bounded plume theories to a discharge plume-resolving LES (MITgcm). We show that these LES results are consistent with previous theories for the along-plume and across-plume profiles of vertical momentum. Finally, we demonstrate that using the wall-bounded plume modifications leads to a 40x factor increase in melt rate prediction for LeConte Glacier, which is necessary for consistency with existing observations.

Future work may test these parameterizations for consistency with other direct observations near vertical ice faces including warm and cold glaciers and icebergs. Additional modeling studies at both the LES and DNS resolution are needed to understand melt plumes, especially for transitions from buoyancy-dominated to shear-dominated bound-

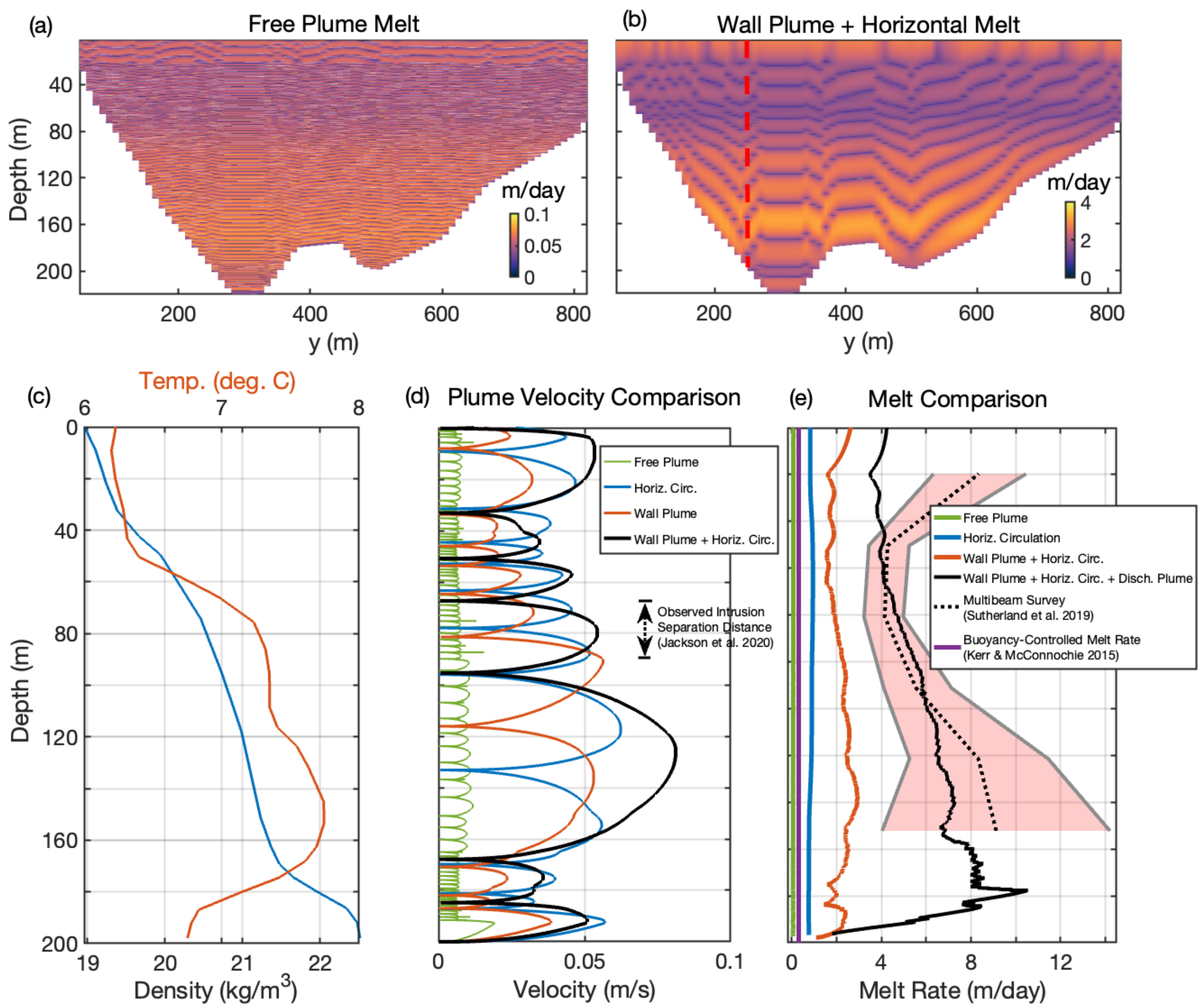

Figure 4. Melt rates at the LeConte glacier face calculated using (a) free plume parameters (Jackson et al., 2019), and (b) wall plume parameters with an additional horizontal circulation melt contribution driven by a uniform horizontal velocity of $v = 0.2$ m/s. Note that the color ranges between panels (a) and (b) differ by a factor of 40. (c) Temperature and salinity profiles from Sutherland et al. (2019) used in the calculations. (d) The plume velocity as a function of depth (assuming a starting depth of 200 m, as in the location dotted red line in panel b) for free plume parameters (green), a free plume with horizontal circulation (blue), wall plume parameters (red), and wall plume parameters with horizontal velocity (black). The observed mid-depth intrusion separation of approx. 20 m in Jackson et al. (2019) is shown for comparison. (e) The meridionally-averaged melt rate for various theories and approximations is shown and compared to the repeat multibeam survey-based estimates from Sutherland et al. (2019). In addition to the cases considered in (d), an additional line discharge plume (with total discharge rate of 220 m^3/s imposed between $y = 250$ m and 350 m) and a buoyancy-controlled boundary layer melt estimate (Kerr & McConnochie, 2015) are shown for comparison.

ary layers and in the presence of both plumes and external velocity forcing. In addition, we may extend these ideas to sloping and geometrically-complex ice-ocean interfaces including ice-shelf cavity geometries, which may also included transition region from near-vertical interfaces to near-horizontal interfaces. Finally, direct observations of the entrainment rate, melt rate, and the boundary layer profiles of both discharge and melt plumes are necessary to improve our understanding of ice-ocean boundaries.

Acknowledgments

The authors would like to thank Dave Sutherland for assistance with the LeConte multibeam data, which is available at: *https://doi.org/10.18739/A22G44*. This material is based in part upon work supported by the National Science Foundation Office of Polar Programs Postdoctoral Fellowship under Grant OPP-2138790, and OPP-2023674. This work used computational resources supported by the NASA FINESST Fellowship under Grant 80NSSC20K163. The MITgcm model configuration and test case is available at: *https://github.com/zhazorken/MITgcm_FJ*.

References

Carroll, D., Sutherland, D. A., Hudson, B., Moon, T., Catania, G. A., Shroyer, E. L., … van den Broeke, M. R. (2016). The impact of glacier geometry on meltwater plume structure and submarine melt in greenland fjords. *Geophys. Res. Lett.*, *43*(18), 9739–9748. doi: 10.1002/2016GL070170

Cowton, T., Slater, D., Sole, A., Goldberg, D., & Nienow, P. (2015). Modeling the impact of glacial runoff on fjord circulation and submarine melt rate using a new subgrid-scale parameterization for glacial plumes. *J. Geophys. Res. Oceans*, *120*, 796–812.

Cowton, T., Sole, A. J., Nienow, P. W., Slater, D. A., & Christoffersen, P. (2018). Linear response of east greenland's tidewater glaciers to ocean/atmosphere warming. *Proc. Natl. Acad. Sci. (USA)*, *115*(31), 7907–7912. doi: 10.1073/pnas.1801769115

Eckert, E., & Jackson, T. (1950). *Analysis of Turbulent Free-Convection Boundary Layer on Flat Plate.* Washington.

Fried, M. J., Catania, G. A., Bartholomaus, T. C., Duncan, D., Davis, M., Stearns, L. A., … Sutherland, D. (2015). Distributed subglacial discharge drives significant submarine melt at a greenland tidewater glacier. *Geophys. Res. Lett.*, *42*(21), 9328–9336. doi: 10.1002/2015GL065806

Gayen, B., Griffiths, R. W., & Kerr, R. C. (2016). Simulation of convection at a vertical ice face dissolving into saline water. *J. Fluid Mech.*, *798*, 284–298.

Grossmann, S., & Lohse, D. (2000). Scaling in thermal convection: a unifying theory. *J. Fluid Mech.*, *407*, 27–56.

Hewitt, I. (2020). Subglacial Plumes. *Annu. Rev. Fluid Mech.*, *52*, 145–169. doi: annurev-fluid-010719-060252

Holland, P. R., Jenkins, A., & Holland, D. M. (2008). The response of ice shelf basal melting to variations in ocean temperature. *J. Climate*, *21*, 2258–2272. doi: 10.1175/2007JCLI1909.1

Jackson, R. H., Nash, J. D., Kienholz, C., Sutherland, D. A., Amundson, J. M., Motyka, R. J., … Pettit, E. (2019). Meltwater intrusions reveal mechanisms for rapid submarine melt at a tidewater glacier. *Geophys. Res. Lett.*. doi: 10.1029/2019GL085335

Jackson, R. H., Shroyer, E. L., Nash, J. D., Sutherland, D. A., Carroll, D., Fried, M. J., … Stearns, L. A. (2017). Near-glacier surveying of a subglacial discharge plume: Implications for plume parameterizations. *Geophys. Res. Lett.*, *44*(13), 6886-6894. doi: 10.1002/2017GL073602

Jenkins, A. (1991). A one-dimensional model of ice shelf-ocean interaction. *J. Geophys. Res. Oceans*, *96*, 20671–20677.

Jenkins, A. (2011). Convection-Driven Melting near the Grounding Lines of Ice Shelves and Tidewater Glaciers. *J. Phys. Oceanogr.*, *41*(12), 2279-2294. doi: 10.1175/JPO-D-11-03.1

Jenkins, A., Dutrieux, P., Jacobs, S., McPhail, S., Perrett, J., Webb, A., & White, D. (2010). Observations beneath Pine Island Glacier in West Antarctica and implications for its retreat. *Nat. Geosci.*, *3*, 468–472.

Josberger, E. G., & Martin, S. (1981). A laboratory and theoretical study of the boundary layer adjacent to a vertical melting ice wall in salt water. *J. Fluid Mech.*, *111*, 439–473. doi: 10.1017/S0022112081002450

Kaimal, J. C., & Finnigan, J. J. (1994). *Atmospheric Boundary Layer Flows: Their Structure and Measurement*. Oxford University Press. Retrieved from `https://doi.org/10.1093/oso/9780195062397.001.0001` doi: 10.1093/oso/9780195062397.001.0001

Kerr, R. C., & McConnochie, C. D. (2015). Dissolution of a vertical solid surface by turbulent compositional convection. *J. Fluid Mech.*, *765*, 211–228. doi: doi:10.1017/jfm.2014.722

Malyarenko, A., Wells, A. J., Langhorne, P. J., Robinson, N. J., Williams, M. J., & Nicholls, K. W. (2020). A synthesis of thermodynamic ablation at ice–ocean interfaces from theory, observations and models. *Ocean Modelling*, *154*, 101692. doi: https://doi.org/10.1016/j.ocemod.2020.101692

Marshall, J. A., Hill, C., Perelman, L., & Heisey, C. (1997). A finite-volume, incompressible navier stokes model for studies of the ocean on parallel computers. *J. Geophys. Res.*, *102 (C3)*, 5753–5766.

McConnochie, C. D., & Kerr, R. C. (2017a). Enhanced ablation of a vertical ice wall due to an external freshwater plume. *J. Fluid Mech.*, *810*, 429–447. doi: doi:10.1017/jfm.2016.761

McConnochie, C. D., & Kerr, R. C. (2017b). Testing a common ice-ocean parameterization with laboratory experiments. *J. Geophys. Res.*, *122*, 5905–5915. doi: doi:10.1002/2017JC012918

McPhee, M. G., Morison, J. H., & Maykut, G. A. (1987). Dynamics and thermodynamics of the ice/upper ocean system in the marginal ice zone of the Greenland Sea. *J. Geophys. Res.*, *92*, 7017–7031.

McPhee, M. G., Morison, J. H., & Nilsen, F. (2008). Revisiting heat and salt exchange at the ice-ocean interface: Ocean flux and modeling considerations. *J. Geophys. Res.*, *113*, C06014. doi: 10.1029/2007JC004383

Morton, B. R., Taylor, G. I., & Turner, J. S. (1956). Turbulent gravitational convection from maintained and instantaneous sources. *Proceedings of the Royal Society of London. Series A. Mathematical and Physical Sciences*, *234*(1196), 1-23. doi: 10.1098/rspa.1956.0011

Paillat, S., & Kaminski, E. (2014). Entrainment in plane turbulent pure plumes. *J. Fluid Mech.*, *755*, R2.

Parker, D. A., Burridge, H. C., Partridge, J. L., & Linden, P. F. (2020). A comparison of entrainment in turbulent line plumes adjacent to and distant from a vertical wall. *J. Fluid Mech.*, *882*, A4. doi: doi:10.1017/jfm.2019.790

Parker, D. A., Burridge, H. C., Partridge, J. L., & Linden, P. F. (2021). Vertically distributed wall sources of buoyancy. Part 1. Unconfined. *J. Fluid Mech.*, *907*, A15. doi: doi:10.1017/jfm.2020.808

Pope, S. B. (2000). *Turbulent flows*. Cambridge University Press. doi: 10.1017/CBO9780511840531

Ramaprian, M. S., B. R. Chandrasekhara. (1989). Measurements in vertical plane turbulent plumes. *Trans. ASME J. Fluids Engng.*, *111*, 69–77.

Sangras, R., Dai, Z., & Faeth, G. M. (2000). Velocity statistics of plane self-preserving buoyant turbulent adiabatic wall plumes. *Trans. ASME J. Heat*

Transfer, *122 (4)*, 693–700.
Schulz, K., Nguyen, A. T., & Pillar, H. R. (2022). An Improved and Observationally-Constrained Melt Rate Parameterization for Vertical Ice Fronts of Marine Terminating Glaciers. *Geophys. Res. Lett.*, *49*(18), e2022GL100654. doi: https://doi.org/10.1029/2022GL100654
Slater, D. A., Straneo, F., Das, S. B., Richards, C. G., Wagner, T. J. W., & Nienow, P. W. (2018). Localized Plumes Drive Front-Wide Ocean Melting of A Greenlandic Tidewater Glacier. *Geophys. Res. Lett.*, *45*(22), 12,350 – 12,358. doi: 10.1029/2018GL080763
Smagorinsky, J. (1963). General circulation experiments with the primitive equations: I. the basic experiment. *Mon. Wea. Rev.*, *91*(3), 99 - 164. doi: https://doi.org/10.1175/1520-0493(1963)091⟨0099:GCEWTP⟩2.3.CO;2
Straneo, F., & Cenedese, C. (2015). The Dynamics of Greenland's Glacial Fjords and Their Role in Climate. *Annu. Rev. Mar. Sci.*, *7*(1), 89-112. doi: 10.1146/annurev-marine-010213-135133
Straneo, F., & Heimbach, P. (2013). North Atlantic Warming and the Retreat of Greenland's Outlet Glaciers. *Nature*, *504*(7478), 36–43. doi: https://doi.org/10.1038/nature12854
Sutherland, D. A., Jackson, R. H., Kienholz, C., Amundson, J. M., Dryer, W. P., Duncan, D., … Nash, J. D. (2019). Direct observations of submarine melt and subsurface geometry at a tidewater glacier. *Science*, *365*(6451), 369–374. doi: 10.1126/science.aax3528
Sutherland, D. A., Straneo, F., & Pickart, R. S. (2014). Characteristics and dynamics of two major Greenland glacial fjords. *J. Geophys. Res. Oceans*, *119*(6), 3767-3791. doi: 10.1002/2013JC009786
Turner, J. S. (1979). *Buoyancy effects in fluids. Cambridge University Press Paperback.*
van den Broeke, M. R., Enderlin, E. M., Howat, I. M., Munneke, P. K., Noël, B. P. Y., van de Berg, W. J., … Wouters, B. (2016). On the recent contribution of the Greenland ice sheet to sea level change. *The Cryosphere*, *10*, 1933–1946. doi: 10.5194/tc-10-1933-2016
Vreugdenhil, C. A., & Taylor, J. R. (2019). Stratification effects in the turbulent boundary layer beneath a melting ice shelf: Insights from resolved large-eddy simulations. *Journal of Physical Oceanography*, *49*(7), 1905 - 1925. Retrieved from `https://journals.ametsoc.org/view/journals/phoc/49/7/jpo-d-18-0252.1.xml` doi: https://doi.org/10.1175/JPO-D-18-0252.1
Wells, A., & Worster, M. (2008). A geophysical-scale model of vertical natural convection boundary layers. , *609*, 111–137. doi: 10.1017/S0022112008002346
Wood, M., Rignot, E., Fenty, I., Menemenlis, D., Millan, R., Morlighem, M., … Seroussi, H. (2018). Ocean-Induced Melt Triggers Glacier Retreat in Northwest Greenland. *Geophys. Res. Lett.*, *45*(16), 8334–8342. doi: 10.1029/2018GL078024
Zhao, K. X., Stewart, A. L., & McWilliams, J. C. (2021). Geometric Constraints on Glacial Fjord–Shelf Exchange. *J. Phys. Oceanogr.*, *51 (4)*, 1223–1246. doi: 10.1175/JPO-D-20-0091.1
Zhao, K. X., Stewart, A. L., & McWilliams, J. C. (2022). Linking Overturning, Recirculation, and Melt in Glacial Fjords. *Geophys. Res. Lett.*, *49*(15), e2021GL095706. doi: https://doi.org/10.1029/2021GL095706
Zhao, K. X., Stewart, A. L., McWilliams, J. C., Fenty, I. G., & Rignot, E. J. (2023). Standing eddies in glacial fjords and their role in fjord circulation and melt. *Journal of Physical Oceanography*, *53*(3), 821 - 840. doi: https://doi.org/10.1175/JPO-D-22-0085.1

Figure 1.

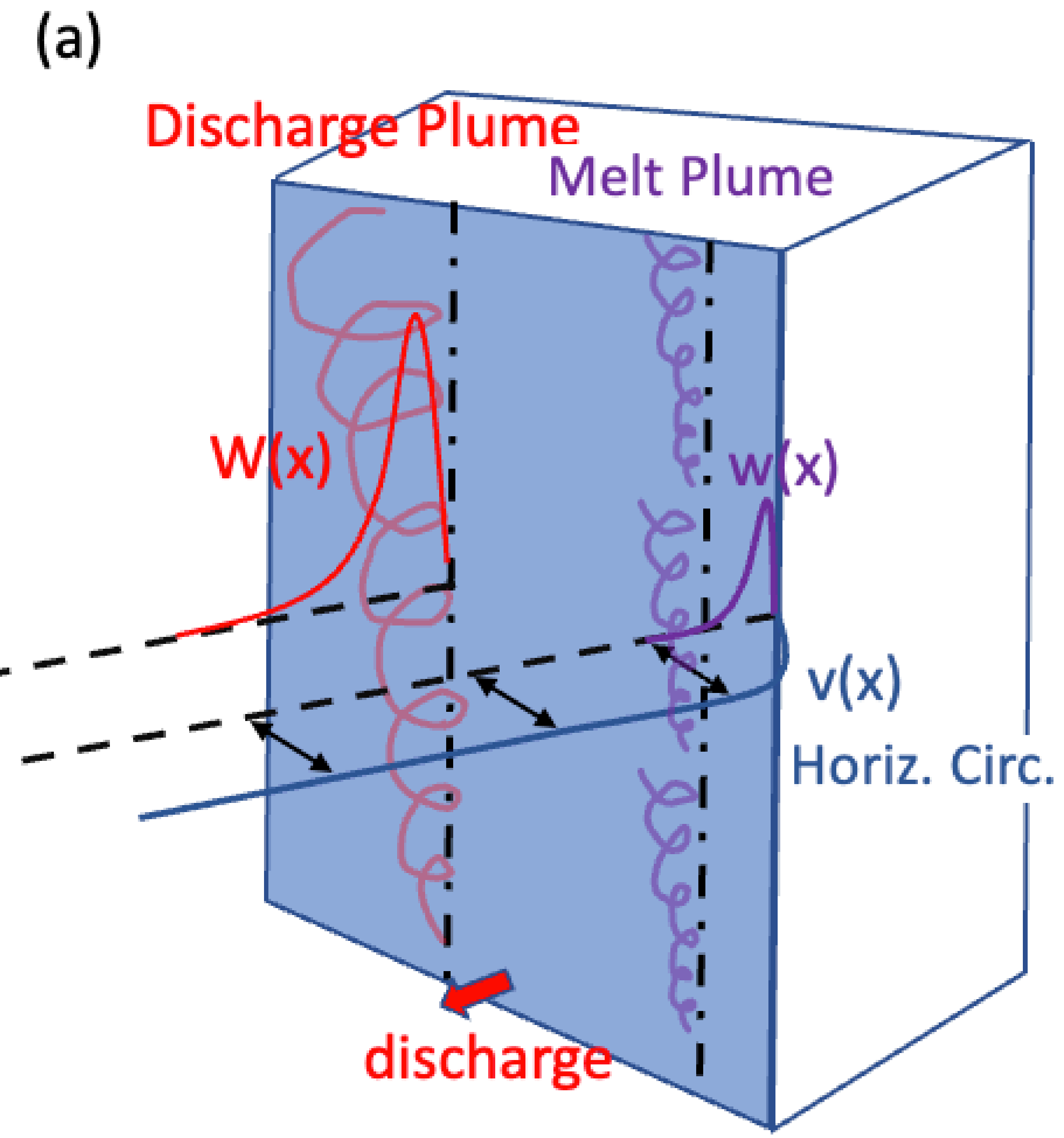

(b)	Drag Coefficient (C_d)	Entrainment (α)	References
Discharge Wall Plume	0.012 - 0.018	0.065 - 0.085	Parker et al. 2021, Greela et al. 1975, Lai et al. 1987, Sangras et al. 2000
Melt Wall Plume	0.12 - 0.18	0.06 - 0.079	Parker et al. 2021, Gayen et al. 2016, Kerr et al. 2015, Cheesewright 1968
Horizontal Circulation	0.0025	-	McPhee et al. 1987, Jenkins 2011, many others
Free Plume (Line)	0.0025	0.10 - 0.13	Jenkins 2011, Cowton et al. 2015, many others

Figure 2.

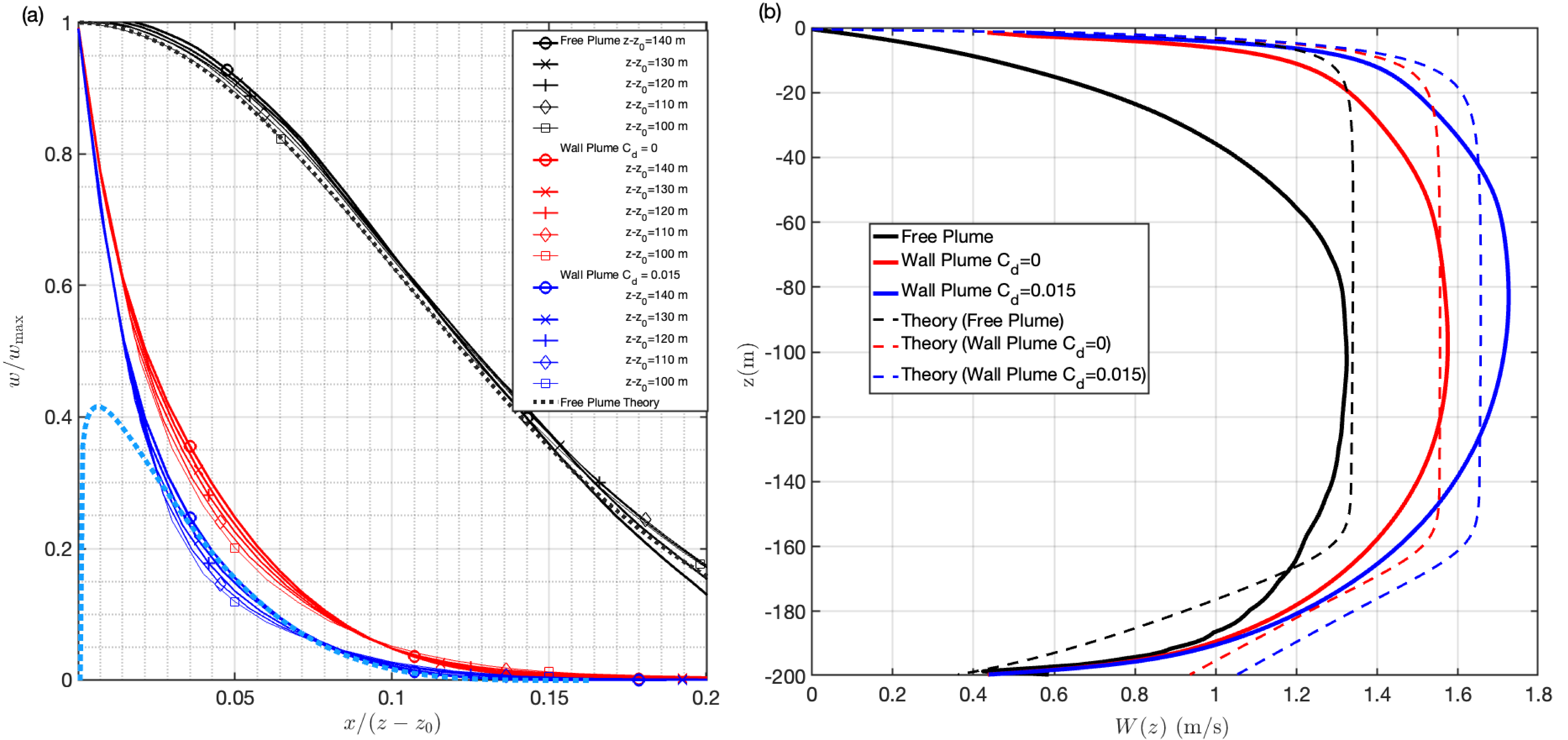

(a)
Free Plume z-z0=140 m
z-z0=130 m
z-z0=120 m
z-z0=110 m
z-z0=100 m
Wall Plume Cd = 0
z-z0=140 m
z-z0=130 m
z-z0=120 m
z-z0=110 m
z-z0=100 m
Wall Plume Cd = 0.015
z-z0=140 m
z-z0=130 m
z-z0=120 m
z-z0=110 m
z-z0=100 m
Free Plume Theory
$w/w_{\max}$
$x/(z-z_0)$
(b)
Free Plume
Wall Plume Cd=0
Wall Plume Cd=0.015
Theory (Free Plume)
Theory (Wall Plume Cd=0)
Theory (Wall Plume Cd=0.015)
z (m)
$W(z)$ (m/s)

Figure 3.

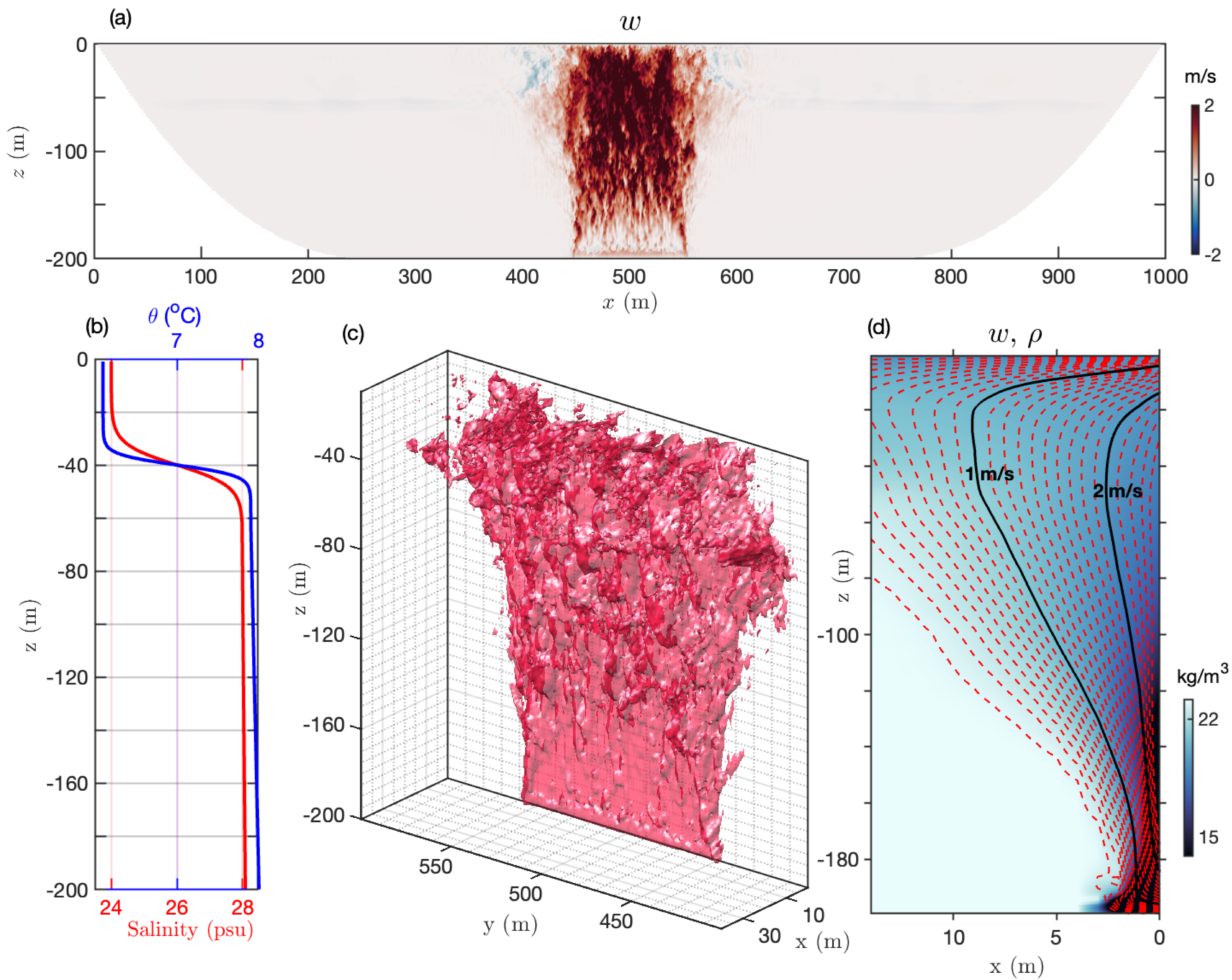

(a)
w
m/s
2
0
-2
0
-100
-200
z (m)
0
100
200
300
400
500
600
700
800
900
1000
x (m)
(b)
θ (°C)
7
8
0
-40
-80
-120
-160
-200
z (m)
24
26
28
Salinity (psu)
(c)
-40
-80
-120
-160
-200
z (m)
550
500
450
y (m)
10
30
x (m)
(d)
$w,\ \rho$
1 m/s
2 m/s
-100
-180
z (m)
kg/m^3
22
15
10
5
0
x (m)

Figure 4.

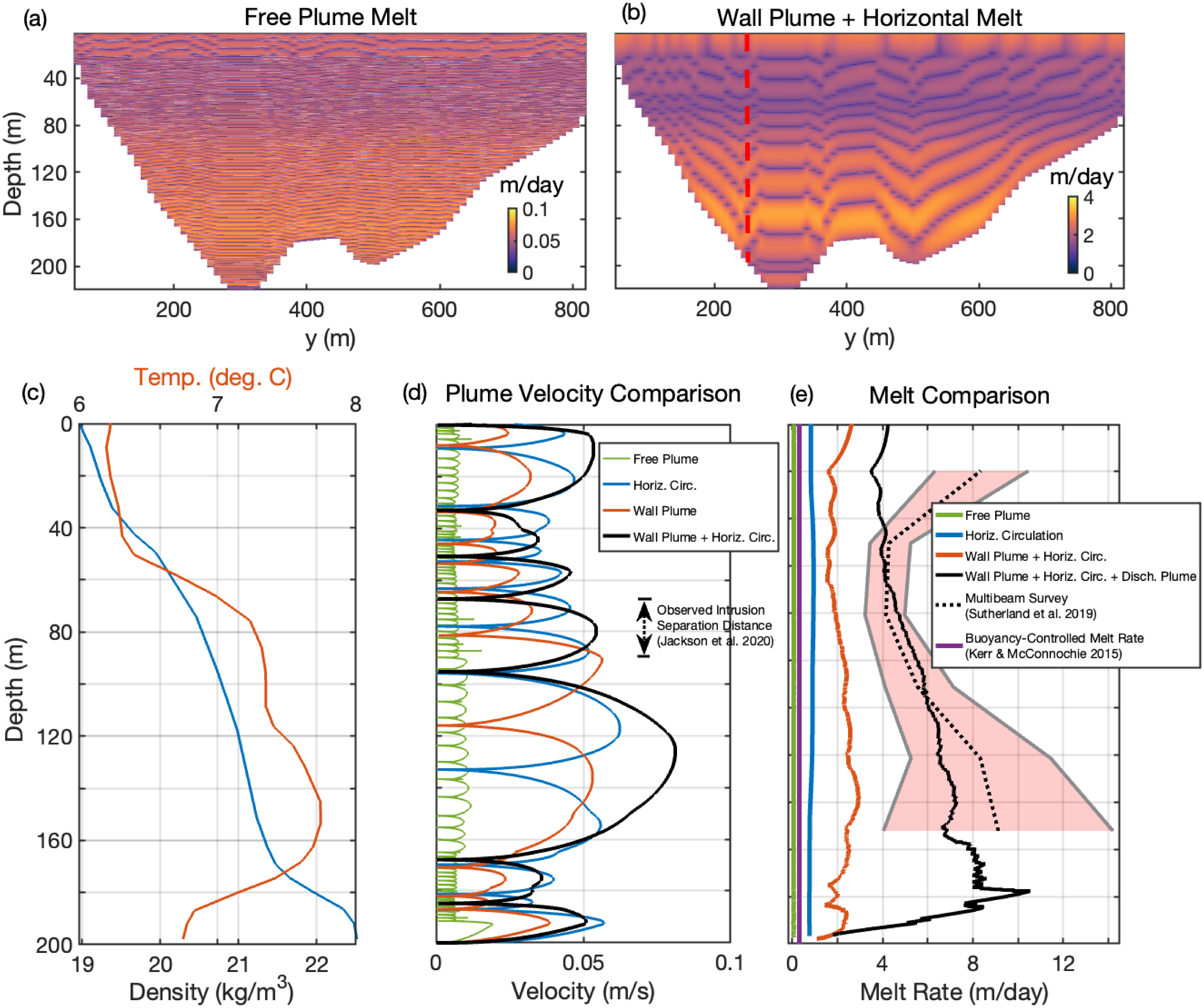

(a)
Free Plume Melt
Depth (m)
y (m)
m/day
(b)
Wall Plume + Horizontal Melt
y (m)
m/day
(c)
Temp. (deg. C)
Depth (m)
Density (kg/m^3)
(d)
Plume Velocity Comparison
Free Plume
Horiz. Circ.
Wall Plume
Wall Plume + Horiz. Circ.
Observed Intrusion
Separation Distance
(Jackson et al. 2020)
Velocity (m/s)
(e)
Melt Comparison
Free Plume
Horiz. Circulation
Wall Plume + Horiz. Circ.
Wall Plume + Horiz. Circ. + Disch. Plume
Multibeam Survey
(Sutherland et al. 2019)
Buoyancy-Controlled Melt Rate
(Kerr & McConnochie 2015)
Melt Rate (m/day)

Supporting Information for "Improved Parameterizations of Vertical Ice-Ocean Interfaces"

Ken X. Zhao[1], Eric D. Skyllingstad[1], and Jonathan D. Nash[1]

[1]College of Earth, Ocean, and Atmospheric Sciences, Oregon State University, 2651 SW Orchard Ave., Corvallis, OR 97331-5503.

Contents of this file

S-1. Wall-Bounded Plume Theory

S-1.1. General Equations for Mass, Momentum, and Buoyancy

The basic formulae for an entraining point or line source plume (representing a discharge plume) and a sheet plume (representing a distributed melt plume) along a wall are revisited in this subsection.

We start with the Boussinesq mass, vertical momentum, and buoyancy equations

$$\frac{\partial u}{\partial x} + \frac{\partial v}{\partial y} + \frac{\partial w}{\partial z} = 0\,, \tag{1a}$$

$$\frac{\partial w}{\partial t} + u\frac{\partial w}{\partial x} + v\frac{\partial w}{\partial y} + w\frac{\partial w}{\partial z} = -\frac{1}{\rho_a}\frac{\partial p}{\partial z} + b + \nu\nabla^2 w\,, \tag{1b}$$

$$\frac{\partial b}{\partial t} + u\frac{\partial b}{\partial x} + v\frac{\partial b}{\partial y} + w\frac{\partial b}{\partial z} = \kappa \nabla^2 b \,, \tag{1c}$$

where $\nu = 1.8 \times 10^{-6}$ m^2/s is the molecular kinematic viscosity and $\kappa \approx \kappa_S = 7.2 \times 10^{-10}$ m^2/s is the molecular scalar diffusivity responsible for buoyancy, which is dominated by salinity near an ice-ocean boundary layer. Here, the vertical velocity $w(x, z, t)$ is in the z-direction along the wall and plume, the horizontal velocity $u(x, z, t)$ is in the x-direction normal to the wall and plume, and the wall is defined to be at $x = 0$. The deviation from hydrostatic pressure is $p(x, z, t)$ and the buoyancy is $b(x, z, t) = g(\rho_a(z) - \rho(x, z, t))/\rho_a$, where ρ is the density of the plume and $\rho_a(z)$ is the far-field density of the ambient fluid. Here, the Boussinesq approximation assumes that $\rho_a - \rho \ll \rho_a$.

We can then decompose the terms in this equation into time-averaged and eddy components for $w(x, z, t) = \overline{w}(x, z) + w'(x, z, t)$ and similarly for the other time-dependent variables. We may also assume that all quantities are independent of the horizontal y-direction so that all ∂_y terms vanish. Assuming a psuedo-steady state with no time-mean tendency terms, the time-mean mass, momentum, and buoyancy equations are

$$\frac{\partial \overline{u}}{\partial x} + \frac{\partial \overline{w}}{\partial z} = 0 \,, \tag{2a}$$

$$\overline{u}\frac{\partial \overline{w}}{\partial x} + \overline{w}\frac{\partial \overline{w}}{\partial z} + \frac{\partial \overline{w'^2}}{\partial z} + \frac{\partial \overline{u'w'}}{\partial x} = -\frac{1}{\rho_a}\frac{\partial \overline{p}}{\partial z} + \overline{b} + \nu\frac{\partial^2 \overline{w}}{\partial x^2} \,, \tag{2b}$$

$$\overline{u}\frac{\partial \overline{b}}{\partial x} + \overline{w}\frac{\partial \overline{b}}{\partial z} + \frac{\partial \overline{u'b'}}{\partial x} + \frac{\partial \overline{w'b'}}{\partial z} = \kappa\frac{\partial^2 \overline{b}}{\partial x^2} \,, \tag{2c}$$

Next, we add boundary conditions to the 2D time-averaged mass, momentum, and buoyancy equations that are appropriate for the wall-bounded plume problem at the wall, the quiescent far-field, and the wall fluxes,

$$\overline{w}(0, z) = \overline{u'w'}(0, z) = \overline{u'b'}(0, z) = 0 \,, \tag{3a}$$

$$\overline{w}(\infty, z) = \overline{u'w'}(\infty, z) = \overline{u'b'}(\infty, z) = 0\,, \tag{3b}$$

$$\overline{u}(0, z) = m,\ \left.\frac{\partial \overline{b}}{\partial x}\right|_{x=0} = \frac{mB}{\kappa}\,, \tag{3c}$$

where $m(z)$ is the wall-source volume flux per unit area (i.e., the sum from melting and subglacial discharge) and mB is the additional wall-source buoyancy flux per unit length for a buoyancy anomaly B.

At the stage, Eqs. (2a)-(3c) fully describe the wall-bounded plume system with a wall source of buoyancy flux. Within the laminar boundary layer (less than a millimeter in the ice-ocean boundary layer), the time time-varying terms are small and we can derive analytical solutions (see Wells and Worster (2008)) for $w(x, z)$, $u(x, z)$ and $b(x, z)$. This is briefly discussed in the next section (on ice-ocean boundary layers). However, in general it is important to understand the profiles of w,u, and b outside of the laminar boundary layers where the eddy covariance terms are comparable and or larger than the molecular viscosity terms (e.g., $\partial_x \overline{u'b'} \geq \kappa \partial_{xx} \overline{b}$ for the buoyancy equation). These eddy covariance terms may then be approximated as eddy viscosity and diffusion terms modeled by appropriate coefficients $\nu_e(x, z), \kappa_e(x, z)$, but currently there are only empirical functions for these functions based on laboratory experiments and DNS of the turbulent boundary layer (e.g., Gayen et al., (2016), Parker et al., (2020), Parker et al., (2021), and many others) rather than closed-form solutions. These empirical functions describe the x-direction variation of w,u, and b, which are further discussed in the next section. However, so far these experiments have mostly been limited to scales of meters and idealized environments rather than geophysical settings and scales. A turbulence closure model for eddy covariance terms at and ice-ocean interface was recently undertaken in Jenkins (2021), and may prove fruitful in the future, but this approach requires observational testing and validation in geophysical contexts, particularly in the case of fast-melting and vertical ice-ocean interfaces.

S-1.2. Plume Theory

In this subsection, we derive the equations for the x-integrated mass, momentum, and buoyancy equations to solve for their z dependency. These equations form the basis for plume theory (see e.g., Morton, Taylor, and Turner (1956)).

To derive these equations, we first integrate Eqs. (2a)-(2c) w.r.t. x,

$$\frac{\partial}{\partial z} \underbrace{\int_0^\infty \overline{w}\, \mathrm{d}x}_{\equiv DW} = - \left. \overline{u} \right|_{x=0}^{\infty} , \tag{4a}$$

$$\frac{\partial}{\partial z} \underbrace{\int_0^\infty \frac{\overline{w}^2}{2}\, \mathrm{d}x}_{\equiv DW^2} + \left. \left[\overline{u}\, \overline{w} + \overline{u'w'} \right] \right|_{x=0}^{\infty} = - \left(\frac{\partial}{\partial z} \int_0^\infty \overline{w'^2} + \frac{1}{\rho_a} \frac{\partial \overline{p}}{\partial z}\, \mathrm{d}x \right) + \underbrace{\int_0^\infty \overline{b}\, \mathrm{d}x}_{\equiv DB} + \nu \left. \frac{\partial \overline{w}}{\partial x} \right|_{x=0}^{\infty} , \tag{4b}$$

$$\frac{\partial}{\partial z} \underbrace{\int_0^\infty \overline{w}\overline{b} + \overline{w'b'}\, \mathrm{d}x}_{\equiv KDWB} + \left. \left[\overline{u}\overline{b} + \overline{u'b'} \right] \right|_{x=0}^{\infty} = \kappa \left. \frac{\partial \overline{b}}{\partial x} \right|_{x=0}^{\infty} , \tag{4c}$$

where we can define a characteristic plume vertical velocity W, buoyancy B, and width D. Note that W is inconsistently defined in the literature, but here we define it as the horizontally-averaged vertical velocity at each depth.

Next we can make the following assumptions based on Morton et al. (1956). The entrainment of ambient fluid is proportional to the characteristic vertical velocity at each depth, $\overline{u}(\infty, z) = -\alpha W$. The first integral on the right hand side of Eq. (4b) is higher order and assumed to be small compared to the other terms. In addition, previous experiments have shown that K (from Eq. (4c) is a constant and is approximately equal to 1 (Parker et al., 2021). We can also make the shear boundary layer approximation $\nu \, \partial_x \overline{w}|_{x=0} = C_d W^2$ with a skin friction coefficient C_d.

Substituting the boundary conditions from Eqs. (3a)-(3c),

$$\frac{\partial(DW)}{\partial z} = \alpha W + m \,, \tag{5a}$$

$$\frac{\partial(DW^2)}{\partial z} = DB - C_D W^2 \,, \tag{5b}$$

$$\frac{\partial(DWB)}{\partial z} = mB \,. \tag{5c}$$

This is now a system of three oridinary differential equations in terms of unknowns W, B, D, m and empirically-derived coefficients for skin friction (C_d) and entrainment (α). If m is known a priori, then this can be integrated numerically. However, since m is the wall-source volume flux per unit area, which includes subglacial discharge (at $z = 0$) and melt rate, this can also be treated as an unknown by adding a fourth equation (either temperature or salinity) or replacing the buoyancy equation with the following equations

$$\frac{\partial(DWT)}{\partial z} = \alpha W T_a + m T_{\mathrm{ef}} \,, \tag{6a}$$

$$\frac{\partial(DWS)}{\partial z} = \alpha W S_a + m S_i \,. \tag{6b}$$

which can be derived analogously to Eqs. (2c) and (3c) for temperature and salinity. Here, T_a and S_a are the ambient temperature and salinity. S_i is the ice interface salinity, and T_{ef} is the effective temperature gradient including latent heat, $T_{\mathrm{ef}} = -c_w^{-1}(L_i + c_i(T_b - T_i))$, where T_b is the bulk boundary layer temperature close to the ice, and T_i is the ice interface temperature. In the context of LeConte glacier, we assume a strongly melting regime (see e.g., Wells and Worster (2008)), so the temperature of the interface is the local freezing temperature, and the interface salinity is assumed to be zero.

To solve for the boundary layer temperature and salinity, and melt rate, we use the three-equation thermodynamics (Hellmer & Olbers, 1989; Holland & Jenkins, 1999), which describes the thermodynamical equilibrium at the ice-ocean interface. This equilibrium can be expressed using approximate heat and salt conservation and the linearized freezing temperature of seawater,

$$m\rho_i(L + c_i(T_b - T_i)) = \rho_w \gamma_T c_w (T - T_b) \tag{7a}$$

$$m\rho_i(S_b - S_i) = \rho_w \gamma_S (S - S_b)\,, \tag{7b}$$

$$T_b = \lambda_1 S_b + \lambda_2 + \lambda_3 z\,, \tag{7c}$$

where ρ_i and ρ_w are the ice and seawater density, respectively, L, c_w, c_i are defined in Section 2, S_p is the plume salinity, S_b is the boundary layer salinity, γ_T and γ_S are the turbulent heat and salt transfer coefficients, respectively, and $\lambda_1 = -5.73 \times 10^{-2}$ °C psu^{-1}, $\lambda_2 = 8.32 \times 10^{-2}$ °C, and $\lambda_3 = 7.61 \times 10^{-4}$ °C m^{-1} are the freezing point slope, offset, and depth. These empirical values are consistent with those used in previous studies (Sciascia et al., 2013; Cowton et al., 2015). Recent parameterizations of the turbulent transfer coefficients (Jenkins et al., 2010) express the turbulent transfer coefficients in terms of near-glacial ocean velocities as

$$\gamma_T = \Gamma_T \sqrt{C_d v^2 + C_d w^2}\,, \tag{8a}$$

$$\gamma_S = \Gamma_S \sqrt{C_d v^2 + C_d w^2}\,, \tag{8b}$$

with C_d, Γ_T, v, w as defined in Section 2, and $\Gamma_S = 6.2 \times 10^{-4}$ is the salt transfer constant. However, an alternative formulation that differentiates between the external and plume-driven shear boundary layers is presented in Section 2 of the main text.

S-2. Model Setup Details

The model used in the study is the Massachusetts Institute of Technology General Circulation Model (MITgcm), which is available at *mitgcm.org*. Using this model, we solve the nonhydrostatic, Boussinesq primitive equations with a 3D Smagorinsky parameterization to set eddy viscosities (Smagorinsky, 1963) and a nonlinear equation of state based on Jackett and McDougall (1995). The MITgcm model configuration is available at: *https://github.com/zhazorken/MITgcm_FJ*.

References

Cowton, T., Slater, D., Sole, A., Goldberg, D., & Nienow, P. (2015). Modeling the impact of glacial runoff on fjord circulation and submarine melt rate using a new subgrid-scale parameterization for glacial plumes. *J. Geophys. Res. Oceans*, *120*, 796–812.

Hellmer, H. H., & Olbers, D. J. (1989). A two-dimensional model for the thermohaline circulation under an ice shelf. *Antarctic Science*, *1*(4), 325–336. doi: 10.1017/S0954102089000490

Holland, D. M., & Jenkins, A. (1999). Modeling Thermodynamic Ice-Ocean Interactions at the Base of an Ice Shelf. *J. Phys. Oceanogr.*, *29*(8), 1787–1800. doi: 10.1175/1520-0485(1999)029⟨1787:MTIOIA⟩2.0.CO;2

Jackett, D. R., & McDougall, T. (1995). Minimal adjustment of hydrographic profiles to achieve static stability. *J. Atmos. Ocean. Technol.*, *14*(4), 381–389.

Jackson, R. H., Nash, J. D., Kienholz, C., Sutherland, D. A., Amundson, J. M., Motyka, R. J., . . . Pettit, E. (2019). Meltwater intrusions reveal mechanisms for rapid submarine melt at a tidewater glacier. *Geophys. Res. Lett.*. doi: 10.1029/2019GL085335

Jenkins, A., Dutrieux, P., Jacobs, S., McPhail, S., Perrett, J., Webb, A., & White, D. (2010). Observations beneath Pine Island Glacier in West Antarctica and implications for its retreat. *Nat. Geosci.*, *3*, 468–472.

Morton, B. R., Taylor, G. I., & Turner, J. S. (1956). Turbulent gravitational convection from maintained and instantaneous sources. *Proceedings of the Royal Society of London. Series A. Mathematical and Physical Sciences*, *234*(1196), 1-23. doi: 10.1098/rspa.1956.0011

Parker, D. A., Burridge, H. C., Partridge, J. L., & Linden, P. F. (2021). Vertically distributed wall sources of buoyancy. Part 1. Unconfined. *J. Fluid Mech.*, *907*, A15. doi: doi:10.1017/jfm.2020.808

Sciascia, R., Straneo, F., Cenedese, C., & Heimbach, P. (2013). Seasonal variability of submarine melt rate and circulation in an East Greenland fjord. *J. Geophys. Res. Oceans*, *118*, 2492–2506.

Wells, A., & Worster, M. (2008). A geophysical-scale model of vertical natural convection boundary layers. , *609*, 111–137. doi: 10.1017/S0022112008002346

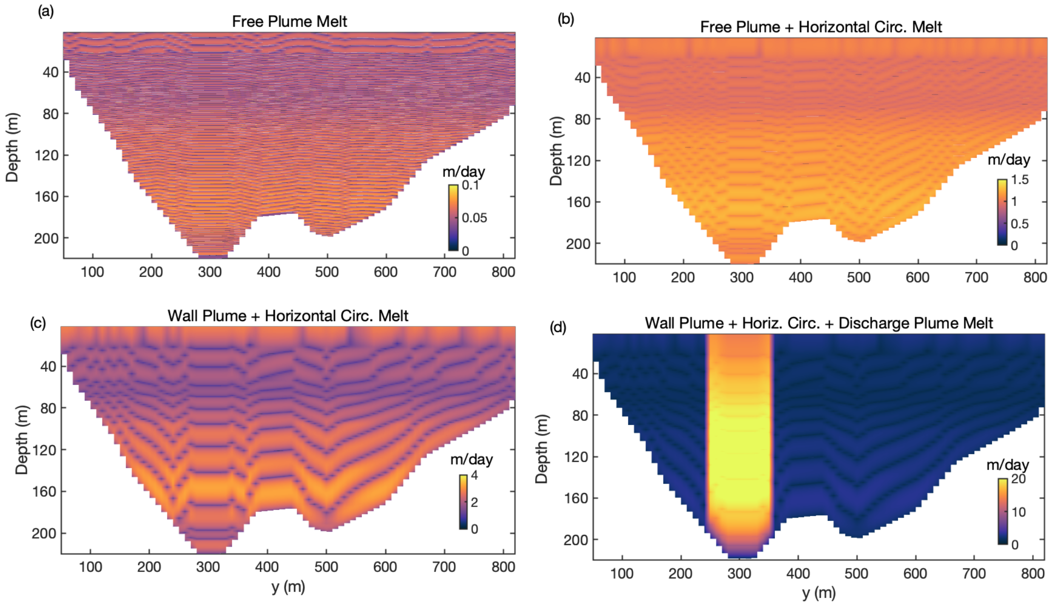

Figure S1. Melt rates at the LeConte glacier face calculated using (a) free plume parameters (Jackson et al., 2019), (b) free plume parameters with an additional horizontal circulation melt contribution driven by a uniform horizontal velocity of $v = 0.2$ m/s, (c) wall plume parameters with the same horizontal circulation melt contribution, and (d) wall plume parameters with the same horizontal circulation melt contribution and a 100-meter wide discharge plume with a discharge rate 220 m^3/s.